Journal of
Materials Chemistry A

ROYAL SOCIETY
OF CHEMISTRY

PAPER

View Article Online
View Journal | View Issue

Check for updates

Cite this: J. Mater. Chem. A, 2020, 8, 5147

Polydopamine/hydroxyapatite nanowire-based bilayered membrane for photothermal-driven membrane distillation†

Sisi Cao,[a] Xuanhao Wu,[b] Yaguang Zhu,[b] Rohit Gupta,[a] Albern Tan,[b] Zhongyang Wang,[b] Young-Shin Jun *[b] and Srikanth Singamaneni *[a]

In developing countries and resource-limited regions, where no power infrastructure or waste heat from industrial plants is available, photothermal-driven membrane distillation (PMD) has been recognized as an attractive and sustainable technology for freshwater generation. PMD enables easy water collection, inherent fouling resistance, low-pressure operation, and high-salinity water treatment. Hydroxyapatite (HA) nanowires with excellent mechanical flexibility owing to their high aspect ratio, low thermal conductivity, easy surface modification and scalable production offer great potential for highly efficient membrane distillation. Herein, we demonstrate that the environmentally benign HA nanowire-based bilayered film offers the highest photothermal efficiency (62%) and water flux (0.89 kg m^{-2} h^{-1}) with 1 sun irradiation (1 kW m^{-2}), among the existing PMD systems without auxiliary heating or multilayer heat recovery reported so far. The hierarchical porous structure formed by the remarkably flexible and intertwined HA nanowires allows low resistance to vapor transport, which is critical for high water flux. Simultaneously, the low thermal conductivity of the thermal insulator layer comprised of HA nanowires prevents conductive heat transfer across the membrane, which significantly enhances the thermal efficiency of the membrane. The completely biocompatible, scalable, and thermally engineered bilayered film demonstrated here achieves highly efficient PMD.

Received 19th November 2019
Accepted 31st January 2020

DOI: 10.1039/c9ta12703h

rsc.li/materials-a

Introduction

Although 71% of the earth surface is covered with water, more than 97% of it is saltwater, and freshwater is limited to only about 2.5%.[1] The water crisis has been exacerbated due to environmental pollution, increased agriculture needs, socio-economic development, and population growth.[2,3] Among various desalination technologies, membrane distillation (MD) has gained wide attention due to its ability to treat highly saline water utilizing waste heat from industrial processes.[4–9] The MD process can be carried out at a lower pressure compared to reverse osmosis (RO) and at a lower temperature than conventional thermal distillation technology.[10–12] In the MD system, the hot feed saline water and cold distillate are present on opposite sides of a porous hydrophobic membrane.[13] Driven by the vapor-pressure gradient caused by the temperature difference, the steam, generated at the interface of the membrane and hot feed water, transports across the membrane to the cold distillate side, where condensation occurs.[14] However, the implementation of conventional MD is hindered in remote regions and disaster-struck communities where low-grade thermal energy from industrial plants and electricity are not readily available.

To address this problem, photothermal-driven membrane distillation (PMD), where MD is integrated with photothermal materials that can effectively convert light to thermal energy, is being proposed.[15–18] In particular, harnessing the abundant sunlight as a source of thermal energy offers great potential to extend it to developing countries and rural communities. Another merit of PMD is the high thermal efficiency compared to the conventional MD process.[19–21] In conventional MD, the conductive heat transfer across the membrane leads to temperature polarization, eventually impairing desalination efficiency.[22,23] Localized surface heating can be achieved on photothermal membranes,[24] which remarkably alleviates the temperature polarization and results in higher thermal efficiency.

Most of the photothermal membranes reported to date employ synthetic polymers, such as polypropylene (PP),[25] polytetrafluoroethylene (PTFE)[26,27] and polyvinylidene fluoride (PVDF),[28–31] as substrates, which are non-biocompatible and non-biodegradable. The disposal of these materials poses a great threat to the environment and ecosystems.[32] Preparation

---

[a] Department of Mechanical Engineering and Materials Science, Institute of Materials Science and Engineering, Washington University in St. Louis, St. Louis, MO, 63130, USA. E-mail: singamaneni@wustl.edu

[b] Department of Energy, Environmental and Chemical Engineering, Washington University in St. Louis, St. Louis, MO, 63130, USA. E-mail: ysjun@wustl.edu

† Electronic supplementary information (ESI) available. See DOI: 10.1039/c9ta12703h

of these membranes *via* precursor polymer powders generally involves toxic organic solvents.[15,33,34] Moreover, incorporation of solar absorbers on the surfaces of these synthetic polymers is not straightforward. To assist the loading of the solar absorbers, the inert surfaces of polymer substrates have been coated with binder materials with sticky functional groups.[23] These concerns associated with utilizing synthetic polymer-based membranes highlight the need for transition to environmentally benign membrane materials and to develop simple and green processes for PMD.

As a major inorganic mineral in the bones and teeth of vertebrates, hydroxyapatite ($Ca_{10}(PO_4)_6(OH)_2$, HA) is well-known for its biocompatibility, biodegradability, and abundance.[35,36] HA nanowires with a high aspect ratio of length to diameter (>100) exhibit remarkable mechanical flexibility,[37] and they can be assembled into a flexible film by simple vacuum filtration. The film possesses an interconnected porous network and allows facile transfer of vapor across the film.[38] Owing to their low thermal conductivity, HA nanowire-based films have been employed as thermal insulators in solar steam generators to enhance localized surface heating.[39] Moreover, the hydrophilicity/hydrophobicity of the HA nanowires can be readily tuned by harnessing hydrogen bonding *via* hydroxyl groups or electrostatic interaction *via* charged moieties (*e.g.*, Ca^{2+} ions), which enables facile surface modification.[40,41] For these reasons, we posit that the biocompatibility, mechanical flexibility, low thermal conductivity, easy processability, and facile surface modification of HA nanowires make them a promising material platform to realize high-performance photothermal membranes for PMD.

Herein, we introduce a highly efficient bilayered photothermal membrane based on HA nanowires with low resistance for vapor transport and high resistance for heat transfer. For this bilayered structure, the top layer comprises polydopamine (PDA)-coated HA (HA@PDA) nanowires to effectively convert solar energy to heat and the bottom layer comprises chitosan (CS)-bonded HA nanowires (HA–CS) as a thermal insulator (Fig. 1). The CS in the bottom layer serves as a bio-degradable molecular glue. The hierarchical structure formed by the highly flexible and intertwined HA nanowires provides a network of channels for facile vapor transport. In addition, the easy surface modification and large surface area of HA nanowires allow dense coating of PDA, which is a highly biocompatible and biodegradable solar absorber.[42–44] More importantly, the HA nanowires with low thermal conductivity can significantly reduce the conductive heat transfer across the membranes and increase the thermal efficiency in PMD. Although bilayered structures have been applied in PMD, the importance of a thermal insulator has not been well studied. Our work represents the first detailed study elucidating the role of the thermal insulation layer in achieving high photothermal efficiency in PMD. This completely environmentally friendly bilayered photothermal film exhibits outstanding light absorption, heat insulation, stability, and porosity, leading to high thermal efficiency in PMD. This work illuminates the great potential of HA nanowires in constructing a high-performance and environmentally friendly photothermal membrane *via* a simple and green processing method.

Results and discussion

The PDA/HA nanowire bilayered film was fabricated by sequential vacuum filtration of HA–CS and HA@PDA nanowires (Fig. 1). The fabrication process is fast and scalable compared to

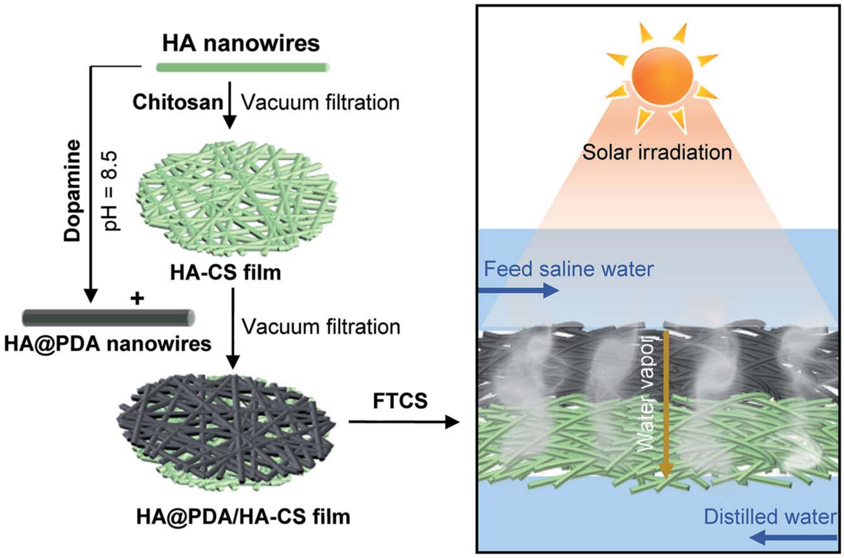

Fig. 1 Schematic illustration depicting the fabrication of the HA@PDA/HA–CS bilayered photothermal film and PMD based on this bilayered structure. Chitosan (CS) is added to the HA nanowire suspension and subsequently the mixture is vacuum filtered to prepare the HA–CS film. HA nanowires are dispersed in dopamine solution (pH = 8.5) to allow the PDA coating on the HA surface and the obtained HA@PDA nanowires were vacuum filtered onto the HA–CS film to prepare the bilayer photothermal film. Finally, to obtain a hydrophobic surface, the film was fluorosilanized using (tridecafluoro-1,1,2,2-tetrahydrooctyl)trichlorosilane (FTCS). PMD was conducted using a direct contact membrane distillation cell under simulated solar irradiation.

freeze-drying and physical/chemical vapor deposition. HA nanowires were synthesized using a previously reported calcium oleate precursor *via* a hydrothermal method, and large-scale synthesis (with a volume up to 100 L) could be achieved using a large stainless-steel autoclave.[41] HA nanowires with a diameter of around 20 nm and high aspect ratio (>100) exhibited remarkable flexibility (Fig. 2A and B). After dispersing in water, a stable wool-like suspension was observed (inset of Fig. 2A). CS, a biopolymer that enables strong interfacial interaction (*e.g.*, hydrogen bonding and electrostatic interaction) with the nanowires, is added to improve the mechanical stability of the HA–CS film.[37]

To fabricate the HA–CS film (thermal insulation layer), the mixture of HA nanowire suspension with 10% (w/w) CS was vacuum filtered. The as-prepared pristine HA–CS film was white (Fig. 2D) and the intertwined nanowires formed an interconnected porous network (Fig. 2E). The pore size of the HA–CS film was analyzed by flow capillary porometry and the mean diameter of the pores was found to be around 200 nm (Fig. 3A). Thermogravimetric analysis (TGA) showed that the loading of CS was around 4% (w/w) for the pristine HA–CS film (Fig. 3B), which was found to be an optimal loading amount for a stable HA–CS film. In contrast, the film fabricated using a mixture of HA nanowire suspension with 5% (w/w) CS could not be successfully peeled from the filter membrane as they broke and disintegrated during the peeling process, suggesting that the HA nanowires are not firmly bound together (Fig. S1†). Higher loading of CS is also detrimental to the PMD performance as it compromises the porosity of the film. Therefore, the optimal loading of CS, which serves as the binding material, is important to ensure mechanical stability of the film and high PMD performance.

In this work, photothermally active PDA was used as the solar absorber, because of its excellent biocompatibility, biodegradability, broadband light absorption and high light-to-heat conversion efficiency.[16,45] To achieve PDA coating, HA nanowires were dispersed in 10 mM Tris–HCl solution (pH = 8.5) followed by the addition of dopamine. PDA was formed *via* oxidative self-polymerization of dopamine and the reaction was stopped after 24 hours. The coating resulted in a color change of the HA nanowire suspension from white (inset of Fig. 2A) to dark brown (inset of Fig. 2F). Transmission electron microscope (TEM) images revealed the ultrathin PDA coating on the HA nanowire surface, and the surface became significantly rougher (Fig. 2G) than that of the pristine HA nanowires (Fig. 2B). The successful coating was confirmed by the PDA nanotubes obtained after dissolving the HA nanowire cores using HCl, and the thickness of the PDA shell was found to be around 15 nm (Fig. S2A†). The isoelectric point (pH_{iep}) of pristine HA nanowires was around 2.3, whereas that of HA@PDA suspension was around 4, which is similar to that of pure PDA and PDA coated

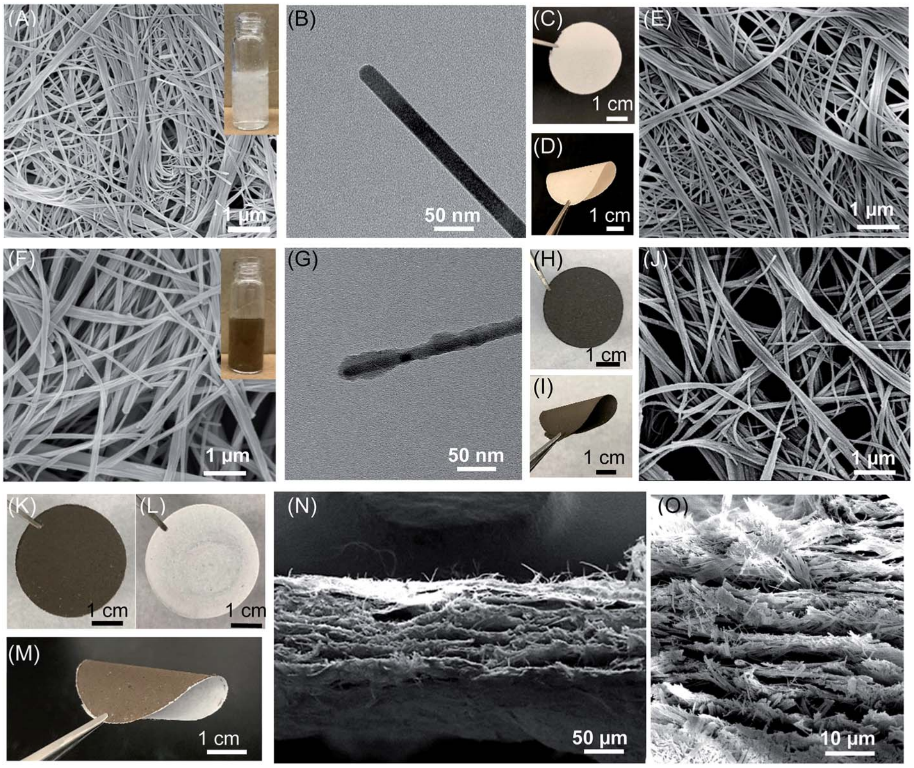

Fig. 2 (A) SEM image of HA nanowires (inset shows the photograph of HA nanowire suspension). (B) TEM image of HA nanowires. Photograph of a flat (C) and deformed (D) HA–CS film. (E) SEM image of the HA–CS film. (F) SEM image of HA@PDA nanowires (inset shows the photograph of HA@PDA nanowire suspension). (G) TEM image of HA@PDA nanowires. Photograph of a flat (H) and deformed (I) HA@PDA film. (J) SEM image of the HA@PDA film. Photograph of the top (K) and bottom (L) of the HA@PDA/HA–CS film and a deformed bilayered film (M). The cross-section SEM images of the HA@PDA/HA–CS film in low magnification (N) and high magnification (O).

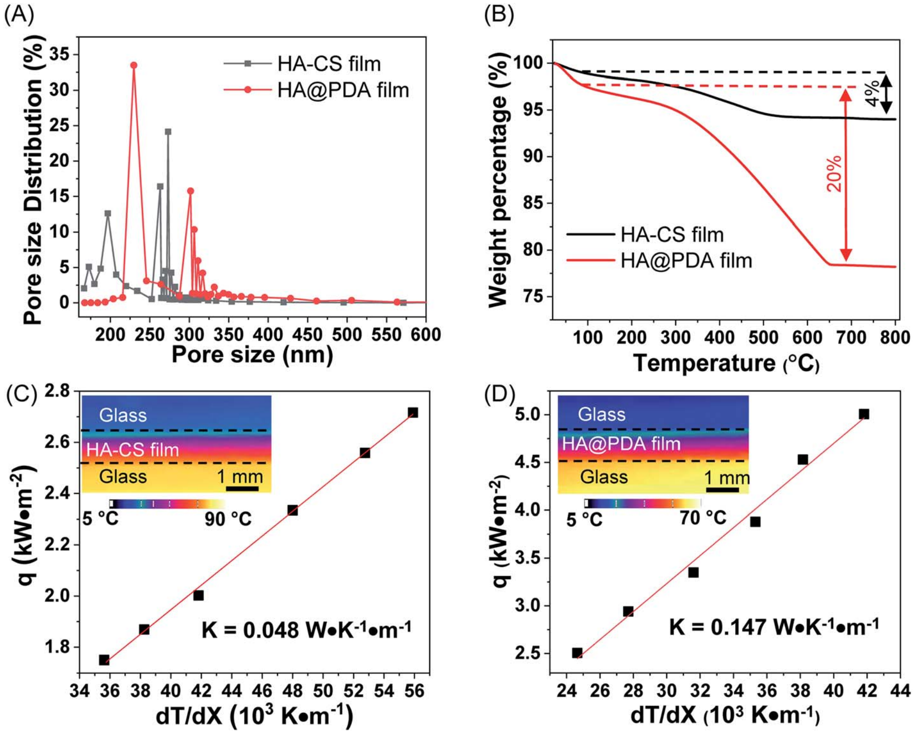

Fig. 3 Characterization of the HA–CS film and HA@PDA film. Pore size distributions (A) and TGA analyses (B) of the representative HA–CS film and HA@PDA film. Thermal conductivity of the HA–CS film (C) and HA@PDA film (D). Insets: representative IR images showing the temperature gradient along the thickness of the HA–CS film (C) and HA@PDA film (D).

surfaces,[46,47] indicating the successful coating of PDA on HA nanowires (Fig. S2B†).

To validate the importance of incorporating the HA–CS layer as a thermal insulator in PMD, a HA@PDA film with the same thickness, consisting of only a solar absorber layer without a thermal insulating layer (HA–CS layer), was fabricated as a comparison. The HA@PDA film was obtained by vacuum filtering the HA@PDA nanowires. In stark contrast with the white color of pristine HA–CS film (Fig. 2C), the HA@PDA film was dark brown (Fig. 2H). The interconnected pores were also observed for the HA@PDA film, with a mean diameter of 230 nm (Fig. 3A). Based on TGA analysis, the weight percentage of PDA in the HA@PDA film was around 20% (Fig. 3B), which was achieved by a 24-hour oxidative self-polymerization of dopamine on HA nanowires. It is important to note that the PDA loading efficiency achieved here is much higher than that reported in the case of hydrophilic PVDF film (9.7%) after seven polymerization cycles (each cycle for 24 hours).[16] The difference is ascribed to the much larger surface area of HA nanowires compared to the porous PVDF membrane. HA nanowires were dispersed in the dopamine solution and provided a significantly larger surface for *in situ* PDA coating compared to the PVDF membrane. Considering that adequate PDA loading is critical for effective light absorption and solar energy harvesting, HA nanowires offer a unique advantage as a template for PDA loading.

To obtain the bilayered HA–CS/HA@PDA film, HA@PDA nanowires were vacuum-filtered on the surface of the HA–CS film (Fig. 1). The color of the upper layer (Fig. 2K) and bottom layer (Fig. 2L) of the as-prepared hybrid film was the same as that of the HA@PDA film and HA–CS film, respectively, which confirmed the bilayered structure. Owing to the mechanical flexibility of the HA nanowires, the HA–CS film, the HA@PDA film, and the bilayered films could be easily bent without inducing brittle fracture (Fig. 2D, I and M). A nacre-like multilayered structure was observed in the cross-section of the bilayered film (Fig. 2N and O) and HA@PDA film (Fig. S3A and B†), resulting from the physical and chemical interactions between the nanowires (*e.g.*, physical entanglements, hydration forces, van der Waals interaction, hydrogen bonding and electrostatic interaction).[40] These available pores and interlayer spacings in the films will provide sufficient channels for effective vapor transport during the PMD operation.

Considering that the heat transfer resistance of the membrane plays a key role in the thermal efficiency of MD, we investigated the thermal conductivity of the HA@PDA film and HA–CS film, which constitute the top and bottom layers of the hybrid film, respectively. The measurements were conducted according to our previously reported method.[48] The film was sandwiched between two glass slides, with the top glass slide in contact with ice and the bottom one in contact with a hot plate, which was employed as the heat source to establish heat flow (the temperature was increased from 70 °C to 120 °C with an interval of 10 °C). The temperature gradient along the cross-section of the film was monitored using an infrared camera (insets of Fig. 3C and D). The thermal conductivity of the HA–CS film was measured to be 0.048 W K^{-1} m^{-1} (Fig. 3C), which is comparable to that of widely used thermal insulator materials for interfacial heating systems, such as polystyrene foam (0.040 W K^{-1} m^{-1}).[49] On the other hand, the HA@PDA film exhibited a thermal conductivity of 0.147 W K^{-1} m^{-1} (Fig. 3D), which is three times higher than that of the HA–CS film. The low thermal conductivity of the HA–CS film makes it an excellent thermal insulator. Under light illumination, the thermal energy is generated in the HA@PDA layer at the top and the HA–CS film at the bottom reduces the conductive heat transfer across the membrane. Therefore, the enhanced heat localization enabled by including the thermal insulator can significantly reduce the temperature polarization, which offers a higher driving force for vapor transport across the membrane and greatly improves the thermal efficiency of the photothermal membrane.

The hydrophobicity of the membrane is critical for the MD process.[8,50–52] In the case of hydrophobic microporous membranes, only vapor can diffuse across the membrane, whereas mass transfer of the liquid phase is prevented. Although the as-prepared HA nanowires are highly hydrophilic, their facile surface modification allows easy hydrophobization. The films were subjected to fluorosilanization using (tridecafluoro-1,1,2,2-tetrahydrooctyl)trichlorosilane (FTCS) to obtain a hydrophobic surface.[53] SEM images confirmed that the porous network was not affected by FTCS treatment (Fig. S5†), and contact angle measurement indicated the successful hydrophobic modification. The original surfaces of the HA–CS film (Fig. S4A†), HA@PDA film (Fig. S4B†) and bilayered films (Fig. S4C and D†) were hydrophilic with water contact angles of 0°; following hydrophobization, the contact angles were 120°, 130°, and 126°, respectively (insets of Fig. S5†).

To investigate the light absorption of the HA@PDA/HA–CS film, the optical transmittance and reflectance of the HA–CS, HA@PDA and HA@PDA/HA–CS films after FTCS treatment are measured and compared (with the film thickness ~70 μm) (Fig. 4A and B). The pristine HA–CS film exhibited high transmittance (~33.3%) and reflectance (~46.2%) in the visible region, implying relatively small light extinction (~20.5%). On the other hand, the HA@PDA film exhibited extremely low light transmittance (~0%) and reflectance (~2.5%), which translated into a large extinction (~97.5%). The difference in optical properties is associated with the presence of PDA, which is known to exhibit broadband light absorption. In addition, the interconnected porous structure of the film causes multiple reflection within the film, enabling high light absorption.[54] Owing to the presence of the HA@PDA layer at the top, the bilayered film also displayed very low light transmittance (~0%) and reflectance (~2.3%), which corresponds to a high light extinction (~97.7%). The bilayer structure of the membrane does not affect the optical properties. Hence, the large optical absorption and excellent light-to-heat conversion efficiency enabled by PDA make the bilayered film a promising membrane for PMD.

Now, we turn our attention to the photothermal conversion efficiency of these films, which critically determines their thermal efficiency for PMD operation. The surface temperature of films in open air was measured using an infrared camera, under simulated solar light illumination at a power density of 1 kW m^{-2} (1 sun) and 9 kW m^{-2} (9 sun) (Fig. 4C). After light irradiation for 120 seconds, the surface temperature of the pristine HA–CS film increased from ~25 °C to ~28 °C at 1 sun irradiation and to ~32 °C at 9 sun irradiation, while the temperature increased to ~43 °C at 1 sun and to ~238 °C at 9 sun illumination for the HA@PDA film (Fig. 4D and E). In the presence of HA–CS as a thermal insulator layer, the surface

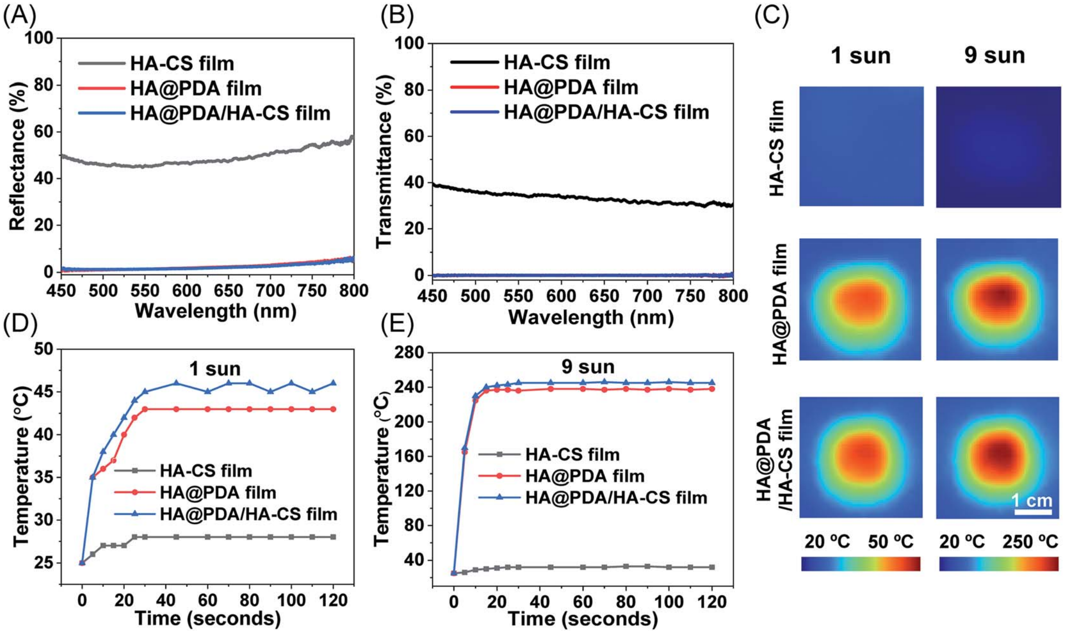

Fig. 4 Optical and photothermal properties of the membranes. Reflectance (A) and transmittance spectra (B) of the HA–CS film, HA@PDA film, and HA@PDA/HA–CS film. (C) IR images showing the surface temperature of the HA–CS film, HA@PDA film and HA@PDA/HA–CS film under 1 sun and 9 sun illumination in open air after 120 seconds. The plots showing the surface temperature of the HA–CS film, HA@PDA film and HA@PDA/HA–CS film under 1 sun (D) and 9 sun illumination (E) as a function of irradiation time.

temperature of the bilayered film increased to ~46 °C at 1 sun irradiation and ~245 °C at 9 sun irradiation. The higher surface temperatures for the bilayered structures, compared to the pure HA@PDA film in the open air, highlight the importance of integrating a thermal insulating layer into the photothermal membrane, which effectively mitigates the heat dissipation and enhances the localized heating at the surface.

The PMD performance of the HA@PDA/HA–CS bilayered film was evaluated in a specially designed direct contact membrane distillation (DCMD) module (Fig. S6†), with a HA@PDA film with the same thickness as a control for comparison (Fig. 5A). The PMD setup was maintained to be the same as our reported test conditions.[16] Simulated seawater, 0.5 M NaCl solution at ambient temperature (20 °C), was used as the feed water. Because the feed water flow rate can affect the water collection as we showed in our previous work,[16] the flow rate was fixed at 3.6 mL min^{-1}, based on our previous work. The distillate at room temperature with a flow rate of 16.2 mL min^{-1} was circulated on the opposite side of the membrane, and the generated freshwater was quantified by measuring the weight increase of the distillate as a function of irradiation time (Fig. 5C) (all tests were conducted for 60 minutes). The water flux for the HA@PDA film was 0.65 kg m^{-2} h^{-1} and 6.16 kg m^{-2} h^{-1} under 1 sun and 9 sun illumination, respectively. On the other hand, for the HA@PDA/HA–CS bilayered film, the water flux was found to be 0.89 kg m^{-2} h^{-1} and 8.28 kg m^{-2} h^{-1} under 1 sun and 9 sun irradiation, respectively. These results indicated that the presence of a thermal insulation layer led to ~27% and ~34% higher water flux compared to the HA@PDA film under 1 sun and 9 sun illumination, respectively.

The thermal efficiency of the photothermal membrane is determined by the ratio of heat flux required to generate distillate flux to the total irradiated solar flux, $\eta = \frac{\dot{m}h_{\text{vap}}}{I}$, where $m^{\cdot}$ represents the distillate flux of water, h_{vap} refers to the total evaporation enthalpy change, and I is the total incident solar flux. Given the water evaporation enthalpy of 2454 kJ kg^{-1} (~0.68 kW kg^{-1} h^{-1}),[23,55] the water flux was 0.65 kg m^{-2} h^{-1} for the HA@PDA film under 1 sun illumination, so the minimum heat flux needed to sustain this distillate flux is 0.45 kW m^{-2} for the HA@PDA film. The total incident solar flux is 1 kW m^{-2}, so the corresponding thermal efficiency of the HA@PDA film is 45%. The distillate flux of the HA@PDA film was 6.16 kg m^{-2} h^{-1} under 9 sun illumination, so the required minimum heat flux is 4.20 kW m^{-2} and the calculated thermal efficiency is 46%. This efficiency is much higher than the previously reported efficiency achieved by carbon black nanoparticle-coated PVDF membrane (~22%). The superior performance is closely related to the high loading of PDA and the hierarchical porous network of the membrane. The large surface area and facile

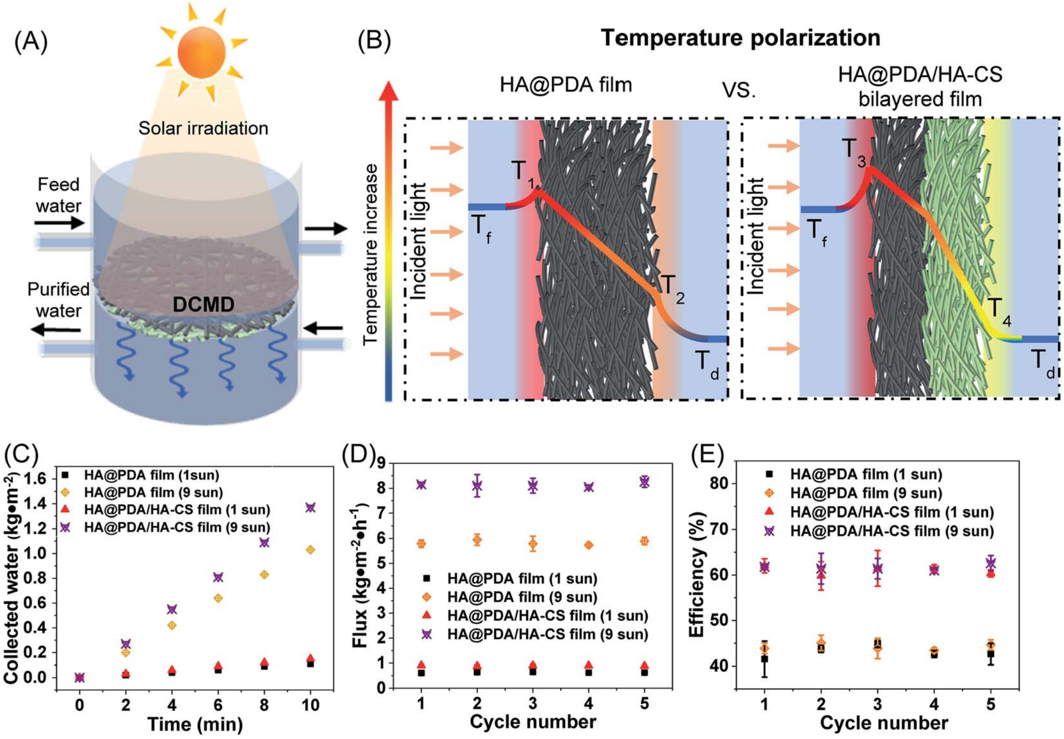

Fig. 5 PMD performance of the HA@PDA film and HA@PDA/HA–CS film. (A) Schematic illustration of photothermal direct contact membrane distillation (DCMD) using HA@PDA/HA–CS film with the thickness of the feed water at 8 mm. (B) Schematic illustration of the thermal profile of DCMD using a HA@PDA film (left) and HA@PDA/HA–CS film (right) under solar irradiation. (C) PMD performance of the HA@PDA film and HA@PDA/HA–CS film in purifying 0.5 M NaCl saline water under 1 sun and 9 sun illumination. Flux (D) and thermal efficiency (E) of the photothermal DCMD system using the HA@PDA film and HA@PDA/HA–CS film, with 0.5 M NaCl saline water under 1 sun and 9 sun irradiation for 5-cycle testing (each cycle for 1 hour, standard deviation obtained from measurements of 3 samples; some of the error bars are hidden by the symbols because the error bars are smaller than symbol sizes).

surface modification of HA nanowires allow a dense and stable coating of PDA, resulting in high thermal energy output from HA@PDA nanowires under light irradiation. Furthermore, the nanowires with high aspect ratio intertwine with each other and form the interconnected porous structure, which results in a low resistance for vapor transport. As for the carbon black nanoparticle-loaded PVDF membrane, a polymeric binder is added to prevent the desorption and leaching of the light-absorbing nanoparticles from the porous matrix, which inevitably narrows the pores and reduces the mass transport.[23,56]

Under identical test conditions, we also evaluated the performance of the HA@PDA/HA–CS bilayered film. The efficiency reached 62% and 63% under 1 sun and 9 sun irradiation, respectively, which is much higher than that of the HA@PDA film and previously reported PDA-coated PVDF membrane (∼45%).[16] This bilayered membrane represents the highest efficiency for PMD among those reported so far, treating the saline water at room temperature without auxiliary heating or heat recovery system.[16,23] The improvement is mainly attributed to the enhanced localized heating at the evaporative surface owing to the presence of the HA–CS thermal insulation layer. Membranes with a high thermal efficiency have a relatively high resistance to conductive heat transfer as well as low resistance to mass transfer.[57] The low thermal conductivity of the HA–CS layer in the hybrid film significantly reduces the conductive heat dissipation across the membrane and remarkably impairs the temperature polarization, yielding a much stronger driving force for vapor transport.

During PMD, the thermal energy generated by the PDA leads to surface heating, so that the temperature of the membrane surface (T_1) is larger than that of feed water (T_f). The generated vapor on the hot surface transfers to the cold distillate side due to the temperature difference between the two sides of the membrane ($T_1 > T_2$). However, the conductive heat transfer across the membrane results in the temperature increase on the permeate side of the membrane (Fig. 5B). The smaller temperature difference across the membrane eventually lowers the driving force for the vapor transfer. In the presence of the HA–CS layer as a thermal insulator, the conductive heat from the hot surface (T_3) to the permeate side (T_4) of the membrane can be greatly reduced (Fig. 5B). Hence, more thermal energy is preserved on the surface for localized heating, and thus a larger temperature difference across the membrane is achieved with the bilayered film, ultimately resulting in higher solar efficiency for PMD.

To evaluate the long-term PMD performance, the HA@PDA film and bilayered film were tested over 5 cycles (each cycle for 1 hour). The average fluxes of the HA@PDA film were 0.63 kg m^{-2} h^{-1} and 5.83 kg m^{-2} h^{-1}, and those of the HA@PDA/HA–CS film were 0.89 kg m^{-2} h^{-1} and 8.13 kg m^{-2} h^{-1}, under 1 sun and 9 sun illumination, respectively (Fig. 5D). The average thermal efficiencies of the HA@PDA film were 43% and 44%, and those of the bilayered film were 61% and 62%, under 1 sun and 9 sun illumination, respectively (Fig. 5E). The performance using both films remained constant during the 5 cycles, and the variations in flux and thermal efficiency were less than 5%. As mentioned above, the anti-wetting property of membranes is critical for the MD process. Therefore, the durability of the hydrophobic modification of the membrane has also been investigated. The contact angle of the HA@PDA film before the PMD test was 129° and it was 125° for the bilayered film after 5-cycle testing (Fig. S7†). The negligible change (variation less than 5%) in the contact angle of the films indicates the durability of hydrophobic modification over repeated use of the membranes. Based on the Cantor–Laplace equation,[58,59] the calculated liquid entry pressures for the HA@PDA film and bilayered film are 110 kPa and 100 kPa, respectively. We then evaluated the mechanical stability of the film. Even after vigorous mechanical agitation for 2 weeks, the bilayered film did not display any signs of disintegration (Fig. S8A†), and no change in morphology and hydrophobicity was observed (Fig. S8B and C†), highlighting the potential for long-term PMD application. This excellent durability of the membrane is ascribed to the outstanding mechanical properties (*e.g.*, high flexibility) of HA nanowires and the intertwined morphology of the network, which serves as mechanical interlocks. In fact, numerous reports in the past demonstrated that the strong interfacial interactions (*e.g.*, hydrogen bonding and electrostatic interactions) of HA nanowires with materials possessing polar functional groups (*e.g.* glass fibers, cellulose fibers, and CS) provide excellent mechanical strength to HA nanowire-based films, which can be used as printing papers,[36] separators for lithium batteries,[38] bone-fracture fixation materials,[37] and fire-alarm wallpapers.[35] Considering the excellent mechanical stability, low thermal conductivity, interconnected porous network, facile surface modification, scalable synthesis and environmentally benign nature, HA nanowire-based membranes are highly comparable to, if not better than, conventional materials for membrane distillation, such as PVDF, PTFE and PP.

Conclusions

Here, we have successfully designed and fabricated a biocompatible HA@PDA/HA–CS bilayered film membrane for highly efficient PMD. The photothermal efficiency of the PDA/HA nanowire film reached 62% under 1 sun illumination and represents the highest efficiency for PMD reported so far for treating saline water at room temperature without any auxiliary heating system or heat recovery system. The facile surface modification and large surface area make HA nanowires an outstanding template for forming a dense, stable, and efficient PDA coating, which in turn ensures broadband light absorption and high light-to-heat conversion. More importantly, the interconnected porous structure, formed by the highly flexible and intertwined nanowires, leads to low resistance to vapor transfer. Simultaneously, the low thermal conductivity of the HA nanowire layer significantly reduces the conductive heat transfer from the evaporative surface to the cold permeate side. This further improved the localized heating and vapor transfer across the membrane. In the presence of the HA nanowire layer as a thermal insulator, the water flux of the bilayered film is ∼27% (under 1 sun) and ∼34% (under 9 sun) higher than that of the HA@PDA film under identical test conditions, respectively. Furthermore, the excellent mechanical robustness of the bilayered film contributes to long-term and stable PMD performance, showing great potential for real-world application. This environmentally benign, highly efficient and mechanically stable HA nanowire-based photothermal membrane is highly promising for freshwater generation in remote regions and disaster-struck communities by utilizing the abundantly available sunlight and saline water.

Experimental methods

Preparation of hydroxyapatite (HA) nanowires

HA nanowires were synthesized by the calcium oleate precursor solvothermal method reported previously.[41] For all experiments, unless otherwise mentioned, we have used deionized water (≥18.2 MΩ cm, Barnstead). Briefly, sodium hydroxide (NaOH, Sigma Aldrich) aqueous solution (1.73 M, 56.3 mL), calcium chloride ($CaCl_2$, Sigma Aldrich) aqueous solution (250 mM, 45 mL), and sodium dihydrogen phosphate dihydrate ($NaH_2PO_4\cdot 2H_2O$, Alfa Aesar) aqueous solution (333 mM, 67.5 mL) were added to a mixture of H_2O (50.6 mL), methanol (22.5 mL) (Sigma Aldrich), and oleic acid (35.1 g) (Sigma Aldrich) under stirring, respectively. Then, the mixture was transferred to a Teflon-lined stainless-steel autoclave (Parr Co., Moline, IL) and maintained at 180 °C for 24 h. The precipitates were centrifuged at 1500 rpm for 5 min and the supernatant was decanted. The collected product was dispersed in a mixture of ethanol (95%, Sigma Aldrich) and deionized water with a volume ratio of 1 to 1. The mixture was centrifuged at 1500 rpm for 5 min, and the supernatant was subsequently removed. This washing step was repeated three times. Finally, the products were dispersed in deionized water and the supernatant was decanted after centrifuging at 4000 rpm for 5 min. The rinsing step was repeated three times and the final products were dispersed in deionized water. To determine the HA concentration, the HA suspension (1 mL) was dried in an oven at 70 °C overnight, and the weight of dry HA was measured.

Preparation of polydopamine (PDA)-coated HA (HA@PDA) nanowires

To ensure the uniform dispersion of HA nanowires in solution, HA nanowires (20 mg) were dispersed in Tris–HCl buffer solution (10 mM, pH = 8.5, 50 mL) followed by sonication for 1 min. Then dopamine (20 mg, Sigma Aldrich) was added to the above suspension, followed by stirring for 24 h in open air to get the homogeneous PDA coating on HA nanowires. Finally, the resultant products were collected, and to remove the salt and PDA nanoparticles, they were washed with deionized water three times by centrifuging at 6000 rpm for 5 min. The collected products were dispersed in deionized water.

Preparation of the HA–CS film, HA@PDA film, and HA@PDA/HA–CS bilayered film

Chitosan (CS) powder (200 mg, Sigma Aldrich) was dispersed in acetic acid (Sigma Aldrich) aqueous solution (1% v/v, 10 mL), and the mixture was kept in an oil bath at 60 °C for 2 h under stirring to obtain a homogeneous solution. The CS solution (20 mg mL^{-1}, 111 μL) was added to an HA nanowire suspension (1 mg mL^{-1}, 20 mL), and the mixture was left on a rotating mixer for 10 min to ensure uniform coating of CS on the HA nanowires. The mixture of CS and HA was homogeneous, and no aggregation was observed. Then, the mixture was vacuum-filtered through a hydrophilic polypropylene (PP) membrane (diameter = 90 mm, pore size = 0.45 μm, Cole-Parmer) to fabricate the HA–CS film. Once all water passed through the filter, the film was dried at 60 °C for 10 min. The HA–CS film was obtained by peeling from the membrane filter.

The HA@PDA film was also obtained by vacuum-filtering HA@PDA nanowire suspension (20 mg) on the PP membrane. To obtain the HA@PDA/HA–CS bilayered film, the above mixture (10 mL) of HA nanowires and CS was vacuum-filtered on the PP membrane. Once all water passed through the filter, the HA@PDA nanowire suspension (1 mg mL^{-1}, 10 mL) was vacuum-filtered on the top surface of the HA–CS film. The film was dried at 60 °C for 10 min and finally the HA@PDA/HA–CS bilayered film was peeled from the membrane filter.

In both membrane preparation procedures, the peeling process does not affect the mechanical strength.

Preparation of PDA hollow nanowires

HCl solution (1 M, Sigma Aldrich) was used to dissolve the HA nanowires from the core of the HA@PDA nanowires. After adding HCl solution to the HA@PDA nanowire suspension, the mixture was vortexed for 5 s and then washed with deionized water three times by centrifuging at 6000 rpm for 10 min. The collected products were dispersed in deionized water.

FTCS treatment

To obtain the hydrophobic surface, the obtained films were treated with (tridecafluoro-1,1,2,2-tetrahydrooctyl)trichlorosilane (Sigma Aldrich) vapor in a sealed container at 70 °C for 24 h. Then, to confirm the hydrophobic surface modification after FTCS treatment, the water contact angle of the films was measured using a contact angle analyzer (Phoenix 300, Surface Electro Optics Co. Ltd).

Nano-/micro-structure characterization

SEM images of the surface and the cross-section of the films and the nanowires were obtained after sputter coating the samples with gold. An FEI Nova 2300 field-emission scanning electron microscope (SEM) was used at an acceleration voltage of 10.5 kV. The transmission electron microscope (TEM) images of nanowires were obtained using a JEOL JEM-2100F field emission microscope. Thermogravimetric analysis (TGA) was performed using a TA Instruments Q5000 IR Thermogravimetric Analyzer in a nitrogen gas flow (at the rate of 10 °C min^{-1}). The pore size distribution of the films was measured using a CFP-LEP-1100A capillary flow porometer. Zeta potential measurements were performed using a Zetasizer Nano ZS (ZEN3600) dynamic light scattering system (Malvern Instruments).

Thermal conductivity measurement

The thermal conductivities of the HA–CS film and HA@PDA film were measured by monitoring the temperature distribution across the thickness of films that were sandwiched between two glass microscope slides. The bottom glass slide was in contact with a hot plate and the top glass slide was in contact with ice. The temperature of the hot plate was increased from 70 °C to 120 °C, in steps of 10 °C. The vertical temperature distribution for the sandwich was monitored using a high-speed IR camera (Telops FAST M3k). The emissivity coefficient of a glass slide and a sample was assumed to be 0.9 to obtain the temperature distribution.[42] The Fourier equation was used to calculate the thermal conductivity of each sample:

$$q' = K\frac{\Delta T}{\Delta X}$$

The heat flux (q') was calculated by assuming the thermal conductivity (K) of 1.05 W $\mathrm{m^{-1}\,K^{-1}}$ for glass slides. Because the glass slide and samples experience the same heat flux, the heat flux value obtained for the glass slide was used to measure the thermal conductivity of the HA–CS film and HA@PDA film samples, respectively.

Optical properties and photothermal performance measurement

Reflectance and transmittance spectra of films were obtained using a CRAIC micro spectrophotometer (QDI 302) coupled to a Leica optical microscope (DM 4000M) with a 20× objective in the range of 450–800 nm with 10 accumulations and 100 ms exposure time in reflection and transmission mode, respectively. The surface temperature of films was monitored using an IR camera (Ti100, Fluke) under light illumination using a solar simulator (Newport 66921 Arc Lamp) under both unfocused irradiation (1 sun) and focused irradiation (9 sun).

Photothermal-driven membrane distillation performance measurement

The PMD performance was evaluated using a direct contact membrane distillation (DCMD) module. The PMD cell was constructed using acrylonitrile butadiene styrene (ABS) plastic by 3D printing. The diameter of the MD cell was 1.5 cm. A Teflon substrate with a thickness of 1 mm was placed between the feed side and distillate side to support the photothermal membrane. 0.5 M NaCl aqueous solution was chosen to simulate the seawater as the feed water and deionized water was chosen as the distillate stream at the bottom of the membrane, both of which were at room temperature (20 °C). The feed and distilled water were continuously circulated using two peristaltic pumps (Welco WPX1-F1 and Stenner 85MHP5), with a flow rate of 3.6 mL $\mathrm{min^{-1}}$ and 16.2 mL $\mathrm{min^{-1}}$, respectively. The thickness of the feed water was maintained at 8 mm. The collected permeate water was recorded using a weight scale (Sartorius ELT402) to measure the weight of the distillate reservoir every 2 min. The light illumination to DCMD was achieved using a solar simulator (Newport 66921 Arc Lamp) under both 1 and 9 sun illumination.

Mechanical agitation

The HA@PDA/HA@CS film (1 cm × 1 cm, $L \times W$) was placed in a 50 mL test tube filled with water, then it was subjected to rigorous mechanical agitation in a tube rotator (VWR Multimix Tube Rotator Mixer 13916-822) for 2 weeks.

Liquid entry pressure calculation

The liquid entry pressure of the HA@PDA and HA@PDA/HA–CS films was calculated based on the Cantor–Laplace equation.[58,60]

$$\mathrm{LEP} = \frac{-2B\gamma_{\mathrm{L}}\cos\theta}{r_{\max}}$$

where LEP is the liquid entry pressure of pure water in Pa, B represents a dimensionless geometrical factor that includes the irregularities of the pores ($B = 1$ for assumed cylindrical pores), γ_{L} refers to the liquid surface tension in N $\mathrm{m^{-1}}$ (in this case water at 20 °C, 0.07286 N $\mathrm{m^{-1}}$), θ represents the contact angle in degrees, and $r_{\max}$ is the maximal pore radius in m (non-closed pore, $r_{\max} = 0.86 \times 10^{-6}$ m according to the measurement of flow capillary porometry).

Conflicts of interest

There are no conflicts to declare.

Acknowledgements

We acknowledge the support from the National Science Foundation Environmental Engineering Program (CBET-1604542). The authors thank the Nano Research Facility (NRF) and Institute for Materials Science and Engineering (IMSE) at Washington University in St. Louis for providing access to characterization facilities. The authors thank Prof. Vijay Ramani of Environmental and Chemical Engineering at Washington University in St. Louis for providing the vacuum filtration setups, and Prof. Xianfeng Wang of Donghua University for providing the capillary flow porometer to characterize the pore size distribution of films.

References

1 D. Ghim, Q. Jiang, S. Cao, S. Singamaneni and Y.-S. Jun, *Nano Energy*, 2018, **53**, 949–957.
2 *The United Nations World Water Development Report 2019: Leaving No One Behind*, 2019.
3 Q. Jiang, D. Ghim, S. Cao, S. Tadepalli, K.-K. Liu, H. Kwon, J. Luan, Y. Min, Y.-S. Jun and S. Singamaneni, *Environ. Sci. Technol.*, 2019, **53**, 412–421.
4 C. Boo and M. Elimelech, *Nat. Nanotechnol.*, 2017, **12**, 501.
5 P. Goh, T. Matsuura, A. Ismail and N. Hilal, *Desalination*, 2016, **391**, 43–60.
6 E. H. Ang, Y. Z. Tan and J. W. Chew, *J. Mater. Chem. A*, 2019, **7**, 10206–10211.
7 A. Deshmukh, C. Boo, V. Karanikola, S. Lin, A. P. Straub, T. Tong, D. M. Warsinger and M. Elimelech, *Energy Environ. Sci.*, 2018, **11**, 1177–1196.

8 R. Long, X. Lai, Z. Liu and W. Liu, *Energy*, 2018, **148**, 1060–1068.

9 Z. Wang, T. Horseman, A. P. Straub, N. Y. Yip, D. Li, M. Elimelech and S. Lin, *Sci. Adv.*, 2019, **5**, eaax0763.

10 K. W. Lawson and D. R. Lloyd, *J. Membr. Sci.*, 1997, **124**, 1–25.

11 A. Alkhudhiri, N. Darwish and N. Hilal, *Desalination*, 2012, **287**, 2–18.

12 T. Y. Cath, V. D. Adams and A. E. Childress, *J. Membr. Sci.*, 2004, **228**, 5–16.

13 L. Camacho, L. Dumée, J. Zhang, J.-d. Li, M. Duke, J. Gomez and S. Gray, *Water*, 2013, **5**, 94–196.

14 M. Gryta, *Membranes*, 2012, **2**, 415–429.

15 A. Politano, P. Argurio, G. Di Profio, V. Sanna, A. Cupolillo, S. Chakraborty, H. A. Arafat and E. Curcio, *Adv. Mater.*, 2017, **29**, 1603504.

16 X. Wu, Q. Jiang, D. Ghim, S. Singamaneni and Y.-S. Jun, *J. Mater. Chem. A*, 2018, **6**, 18799–18807.

17 Y.-S. Jun, X. Wu, D. Ghim, Q. Jiang, S. Cao and S. Singamaneni, *Acc. Chem. Res.*, 2019, **52**, 1215–1225.

18 E. Chiavazzo, M. Morciano, F. Viglino, M. Fasano and P. Asinari, *Nature Sustainability*, 2018, **1**, 763–772.

19 Y.-S. Jun, D. Ghim, X. Wu, S. Cao and S. Singamaneni, *HDIAC Journal*, 2019, **6**, 6.

20 S. Cao, Q. Jiang, X. Wu, D. Ghim, H. Gholami Derami, P.-I. Chou, Y.-S. Jun and S. Singamaneni, *J. Mater. Chem. A*, 2019, **7**, 24092–24123.

21 W. Wang, Y. Shi, C. Zhang, S. Hong, L. Shi, J. Chang, R. Li, Y. Jin, C. Ong, S. Zhuo and P. Wang, *Nat. Commun.*, 2019, **10**, 3012.

22 A. Politano, G. Di Profio, E. Fontananova, V. Sanna, A. Cupolillo and E. Curcio, *Desalination*, 2019, **451**, 192–199.

23 P. D. Dongare, A. Alabastri, S. Pedersen, K. R. Zodrow, N. J. Hogan, O. Neumann, J. Wu, T. Wang, A. Deshmukh, M. Elimelech, Q. Li, P. Nordlander and N. J. Halas, *Proc. Natl. Acad. Sci. U. S. A.*, 2017, **114**, 6936–6941.

24 X. Han, W. Wang, K. Zuo, L. Chen, L. Yuan, J. Liang, Q. Li, P. M. Ajayan, Y. Zhao and J. Lou, *Nano Energy*, 2019, **60**, 567–575.

25 Y. Shao, M. Han, Y. Wang, G. Li, W. Xiao, X. Li, X. Wu, X. Ruan, X. Yan and G. He, *J. Membr. Sci.*, 2019, **579**, 240–252.

26 S. Tadepalli, H. Hamper, S. H. Park, S. Cao, R. R. Naik and S. Singamaneni, *ACS Biomater. Sci. Eng.*, 2016, **2**, 1084–1092.

27 L. Huang, J. Pei, H. Jiang and X. Hu, *Desalination*, 2018, **442**, 1–7.

28 Y. Liao, R. Wang and A. G. Fane, *Environ. Sci. Technol.*, 2014, **48**, 6335–6341.

29 T. Chen, A. Soroush and M. S. Rahaman, *Ind. Eng. Chem. Res.*, 2018, **57**, 14535–14543.

30 Y. Z. Tan, H. Wang, L. Han, M. B. Tanis-Kanbur, M. V. Pranav and J. W. Chew, *J. Membr. Sci.*, 2018, **565**, 254–265.

31 L. Han, Y. Z. Tan, C. Xu, T. Xiao, T. A. Trinh and J. W. Chew, *J. Membr. Sci.*, 2019, **588**, 117196.

32 D. Hou, T. Li, X. Chen, S. He, J. Dai, S. A. Mofid, D. Hou, A. Iddya, D. Jassby, R. Yang, L. Hu and Z. J. Ren, *Sci. Adv.*, 2019, **5**, eaaw3203.

33 H. Ye, X. Li, L. Deng, P. Li, T. Zhang, X. Wang and B. S. Hsiao, *Ind. Eng. Chem. Res.*, 2019, **58**, 3269–3281.

34 Q. Huang, S. Gao, Y. Huang, M. Zhang and C. Xiao, *J. Membr. Sci.*, 2019, **582**, 203–210.

35 F.-F. Chen, Y.-J. Zhu, F. Chen, L.-Y. Dong, R.-L. Yang and Z.-C. Xiong, *ACS Nano*, 2018, **12**, 3159–3171.

36 B. Q. Lu, Y. J. Zhu and F. Chen, *Chem.–Eur. J.*, 2014, **20**, 1242–1246.

37 T. W. Sun, Y. J. Zhu and F. Chen, *Chem.–Eur. J.*, 2017, **23**, 3850–3862.

38 H. Li, D. Wu, J. Wu, L. Y. Dong, Y. J. Zhu and X. Hu, *Adv. Mater.*, 2017, **29**, 1703548.

39 D.-D. Qin, Y.-J. Zhu, F.-F. Chen, R.-L. Yang and Z.-C. Xiong, *Carbon*, 2019, **150**, 233–243.

40 F.-F. Chen, Y.-J. Zhu, Z.-C. Xiong, T.-W. Sun and Y.-Q. Shen, *ACS Appl. Mater. Interfaces*, 2016, **8**, 34715–34724.

41 Z. C. Xiong, Y. J. Zhu, D. D. Qin, F. F. Chen and R. L. Yang, *Small*, 2018, **14**, 1803387.

42 Q. Jiang, H. G. Derami, D. Ghim, S. Cao, Y.-S. Jun and S. Singamaneni, *J. Mater. Chem. A*, 2017, **5**, 18397–18402.

43 L. Zong, M. Li and C. Li, *Nano Energy*, 2018, **50**, 308–315.

44 X. Wu, G. Y. Chen, W. Zhang, X. Liu and H. Xu, *Adv. Sustainable Syst.*, 2017, **1**, 1700046.

45 H. Gholami Derami, Q. Jiang, D. Ghim, S. Cao, Y. J. Chandar, J. J. Morrissey, Y.-S. Jun and S. Singamaneni, *ACS Appl. Nano Mater.*, 2019, **2**, 1092–1101.

46 J. Feng, H. Fan, D.-a. Zha, L. Wang and Z. Jin, *Langmuir*, 2016, **32**, 10377–10386.

47 G. Pérez-Mitta, J. S. Tuninetti, W. Knoll, C. Trautmann, M. E. Toimil-Molares and O. Azzaroni, *J. Am. Chem. Soc.*, 2015, **137**, 6011–6017.

48 Q. Jiang, L. Tian, K. K. Liu, S. Tadepalli, R. Raliya, P. Biswas, R. R. Naik and S. Singamaneni, *Adv. Mater.*, 2016, **28**, 9400–9407.

49 H. Ghasemi, G. Ni, A. M. Marconnet, J. Loomis, S. Yerci, N. Miljkovic and G. Chen, *Nat. Commun.*, 2014, **5**, 4449.

50 H. Chamani, T. Matsuura, D. Rana and C. Q. Lan, *J. Membr. Sci.*, 2019, **572**, 332–342.

51 C. Li, X. Li, X. Du, T. Tong, T. Y. Cath and J. Lee, *ACS Appl. Mater. Interfaces*, 2019, **11**, 18456–18465.

52 M. Sun, C. Boo, W. Shi, J. Rolf, E. Shaulsky, W. Cheng, D. L. Plata, J. Qu and M. Elimelech, *Adv. Funct. Mater.*, 2019, **29**, 1903125.

53 M. E. Leitch, C. Li, O. Ikkala, M. S. Mauter and G. V. Lowry, *Environ. Sci. Technol. Lett.*, 2016, **3**, 85–91.

54 P. Wang, *Environ. Sci.: Nano*, 2018, **5**, 1078–1089.

55 F. Woodward and J. Sheehy, *Principles and Measurements in Environmental Biology*, Elsevier, 2017.

56 J. Wu, K. R. Zodrow, P. B. Szemraj and Q. Li, *J. Mater. Chem. A*, 2017, **5**, 23712–23719.

57 X. An, G. Xu, B. Xie and Y. Hu, *J. Mater. Chem. A*, 2019, **7**, 2376–2384.

58 S. S. Ray, S.-S. Chen, C. T. Ngoc Dan, H.-T. Hsu, H.-M. Chang, N. C. Nguyen and H.-T. Nguyen, *RSC Adv.*, 2018, **8**, 1808–1819.

59 A. Franken, J. Nolten, M. Mulder, D. Bargeman and C. Smolders, *J. Membr. Sci.*, 1987, **33**, 315–328.

60 A. C. M. Franken, J. A. M. Nolten, M. H. V. Mulder, D. Bargeman and C. A. Smolders, *J. Membr. Sci.*, 1987, **33**, 315–328.